


RESEARCH ARTICLE | AUGUST 02 2023

Ultra-stretchable active metasurfaces for high-performance structural color

Amir Ghasemi ; Rui Fang ; Dagou A. Zeze ; Mehdi Keshavarz Hedayati  

AIP Advances 13, 085004 (2023)

<https://doi.org/10.1063/5.0156782>View
OnlineExport
Citation

CrossMark

Articles You May Be Interested In

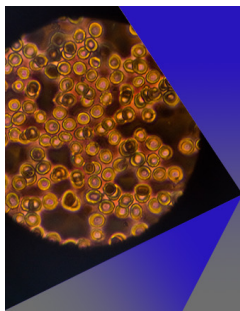
Architected hierarchical kirigami metallic glass with programmable stretchability

AIP Advances (March 2022)

Biaxial stretchable light-emitting device using kirigami-elastomer structure

AIP Advances (November 2022)

Kirigami stretchable strain sensors with enhanced piezoelectricity induced by topological electrodes

Appl. Phys. Lett. (June 2018)

AIP Advances

Special Topic: Medical Applications of Nanoscience and Nanotechnology

Submit Today! AIP
Publishing

Ultra-stretchable active metasurfaces for high-performance structural color

Cite as: AIP Advances 13, 085004 (2023); doi: 10.1063/5.0156782

Submitted: 10 July 2023 • Accepted: 11 July 2023 •

Published Online: 2 August 2023



Amir Ghasemi,  Rui Fang,  Dagou A. Zeze,  and Mehdi Keshavarz Hedayati^{a)} 

AFFILIATIONS

Department of Engineering, Durham University, Durham DH1 3LE, United Kingdom

^{a)} Author to whom correspondence should be addressed: mehdi.keshavarz-hedayati@durham.ac.uk

ABSTRACT

Metamaterials as artificially structural materials exhibit customized properties unattainable in nature. While dynamic response is highly desired, metamaterials are usually passive and cannot be tuned post-fabrication. A conventional active metamaterial consists of rigid resonators mounted on flexible substrates that permit a limited amount of mechanical tuning. Given that rigid resonators permanently deform or debond under large strains (above 30%), the range of flexibility that is possible with tunable metamaterials is limited. Here, we propose a kirigami-inspired geometry that overcomes this limitation. The proposed design enhances stretchability exceeding 100% when compared with the existing design. A high degree of flexibility is achieved through “stress engineering” at the interface between rigid resonators and flexible substrates. Our design shows that the resonance modes shift at a rate of 3.32 ± 0.1 nm for every 1% change in strain, which is the highest tunability reported thus far. We demonstrate how this new concept can be applied to structural color. Using a single design, we demonstrated the full range of colors for the first time. The novel concept of highly stretchable metamaterials may revolutionize the field and enable its use in applications such as wearable sensors, smart displays, and switchable devices requiring extremely dynamic properties.

© 2023 Author(s). All article content, except where otherwise noted, is licensed under a Creative Commons Attribution (CC BY) license (<http://creativecommons.org/licenses/by/4.0/>). <https://doi.org/10.1063/5.0156782>

I. INTRODUCTION

Metamaterials (MMs) are engineered structures with unprecedented properties such as cloaking, negative refraction, perfect absorption, flat lenses, and sub-diffraction printing. In optical metamaterials (OMMs), meta-atoms (i.e., cell units) are smaller than the wavelength of light, yet they still interact with it efficiently.¹ Conventional OMMs provide static and predefined optical functions that are normally controlled by the shape, size, geometry, and arrangements of meta-atoms.² However, dynamic control of the interaction of electromagnetic waves and nanostructures has been a long-standing challenge in optics.³ In particular, the development of reversible and programmable OMMs remains a challenge.⁴ Optical tuning can be achieved by relocating the resonators' spatial position since the optical response is dependent on their location.⁵ Various external stimuli-responsive systems, such as magnetic tuning,⁶ thermal tuning,⁷ optical excitation,⁸ electrochemical tuning,⁹ mechanical tuning,^{10–12} electrical actuation,^{13,14} chemical reactions,^{14,15} etc., have been employed to make this tuning possible.

One of the most popular and studied classes of tunable OMMs is the design that involves placing resonators on flexible substrates.

In this case, the substrate's flexibility is used to dynamically change the inter-resonators' distances and hence tuning the optical responses (transmission and reflectance).^{11,16–18} There is a fundamental limitation to such bi-material structures. Given the large mismatch between the maximum range of elasticity of the elastomeric substrate and the resonators (e.g., metals and high refractive index dielectrics), the stretchability of the proposed devices is very limited. Theoretically, the elastic strain limit in ideal crystalline metals can be up to 10%.¹⁹ However, that of most bulk metals is less than 7% due to the inelastic relaxation of defects such as dislocation, stress-induced phase transformation, and deformation twinning.²⁰ For instance, the elastic strain limit of the typical components used in flexible devices, namely, copper, gold, silicon, and aluminum is 2.8%, 1.9%, 2%, and 1.27%, respectively.^{21–23}

Figure 1(a) compares the mechanical deformation of a metallic film in both a free-standing structure and a bi-material one where the film is bonded to a flexible substrate. When the former structure is strained beyond the elastic limit, a localized necking occurs, and the sample is permanently deformed. However, the study of mechanical deformation and fracture behavior of a bi-material structure under an external load seems more compli-

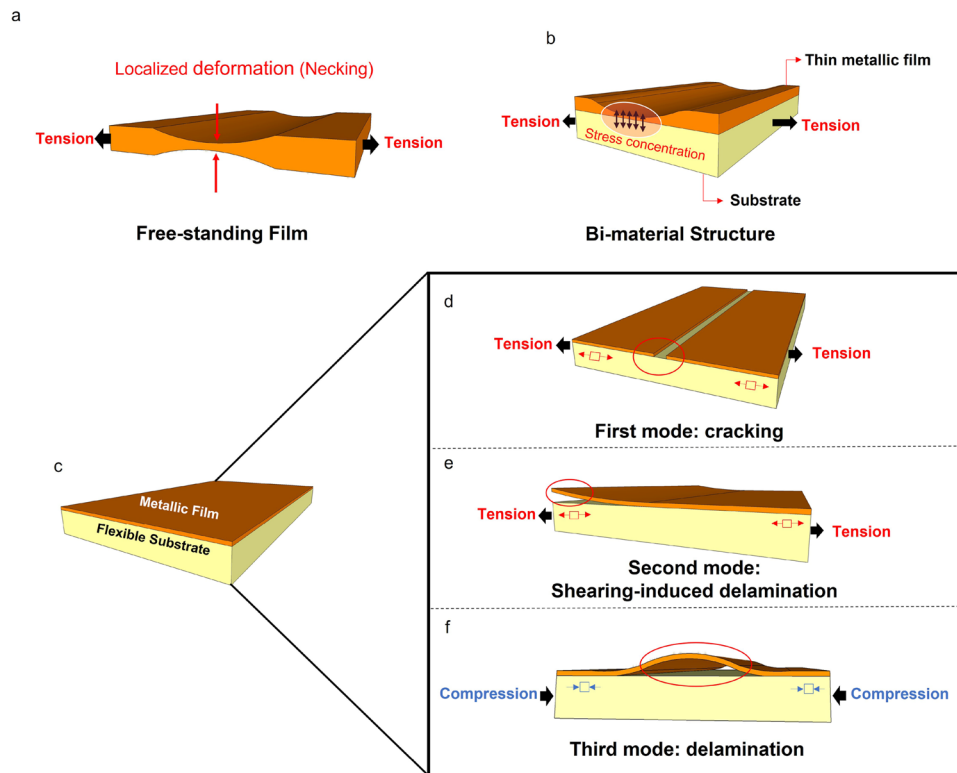


FIG. 1. Schematic of general deformation of a (a) freestanding and (b) bi-material structure under mechanical strains. (c) Bi-layer structure comprising a rigid metallic film/soft substrate and typical failure modes including (d) cracking mode, (e) shearing-induced delamination under tensile load, and (f) delamination under compression load.

cated since a combination of various phenomena, such as cracking, necking, buckling, and delamination, occurs.²⁴

Since the required space for the plastic deformation is unavailable in a substrate-bonded film subjected to a tensile strain, the strain field in the metal film is delocalized,²⁵ allowing the film to permanently deform at a lower strain level and reducing the film's rupture far beyond that of a freestanding film.²⁶

There are a number of ways in which a bi-material structure can deform, as shown in Figs. 1(d)–1(f), which depend heavily on the shape, dimensions, and mechanical properties of both the rigid film and the soft substrate. The first mode occurs when the applied uniaxial stress exceeds the point where further homogeneous deformation is not possible. As a result, a series of strain-induced cracks form perpendicular to the applied stress [cf. Fig. 2(d)], and these cracks propagate, causing the structure to fracture.²⁷

Due to a difference in the normal stress level at the interface, the rigid component experiences shearing stress on its edge in the second mode. According to Fig. 1(e), delamination occurs when this shearing stress reaches the maximum shearing strength of the interface. Finally, when a rigid/soft structure is compressed, rigid film buckles, causing delamination. A high bonding strength postpones the massive buckling in the structure; however, the wavelike buckling pattern on the surface is inevitable²⁸ [cf. Fig. 1(f)].

There are almost no rigid-soft materials that do not exhibit this phenomenon, and MMs are no exception. Therefore, regard-

less of the substrate's rubberiness, the metamaterial's deformability is limited by its intrinsic resonator properties. Since resonators are in direct contact with flexible substrates, external forces directly affect them. Therefore, such flexible MMs rarely reach elongations beyond 30%, far below the maximum elastic deformation of constituent elastomers^{11,12,17,29} (cf. Table I).

Despite success in the design of stretchable devices comprising rigid and soft components in serpentine or horseshoe geometry,³⁵ nanocomposite-based structures,³⁶ and ultrathin flexible substrates,³⁷ proposing an appropriate structure to avoid the emergence of large cracks in a certain strain range (usually falling within 20%–50%) has remained a challenge.³⁸

Mechanical MMs are a quite well-developed class of functional materials that show exceptional properties such as negative values of mechanical and thermomechanical properties including effective mass density,³⁹ Poisson's ratio,⁴⁰ thermal expansion,⁴¹ vanishing shear modulus,⁴² and compressibility. Origami and kirigami-based patterns, a particular subgroup of mechanical MMs, have drawn attention as a technique to design reconfigurable robots,⁴³ reprogrammable deployable structures,⁴⁴ and lightweight metamaterials.⁴⁵ It consists of flexible sections (kirigami connections and origami folds), as well as stiff sections (flat parts between folds and cuts). This design provides a wide range of mechanical properties by varying degrees of flexibility and rigidity without relying heavily on material or dimension.⁴⁶

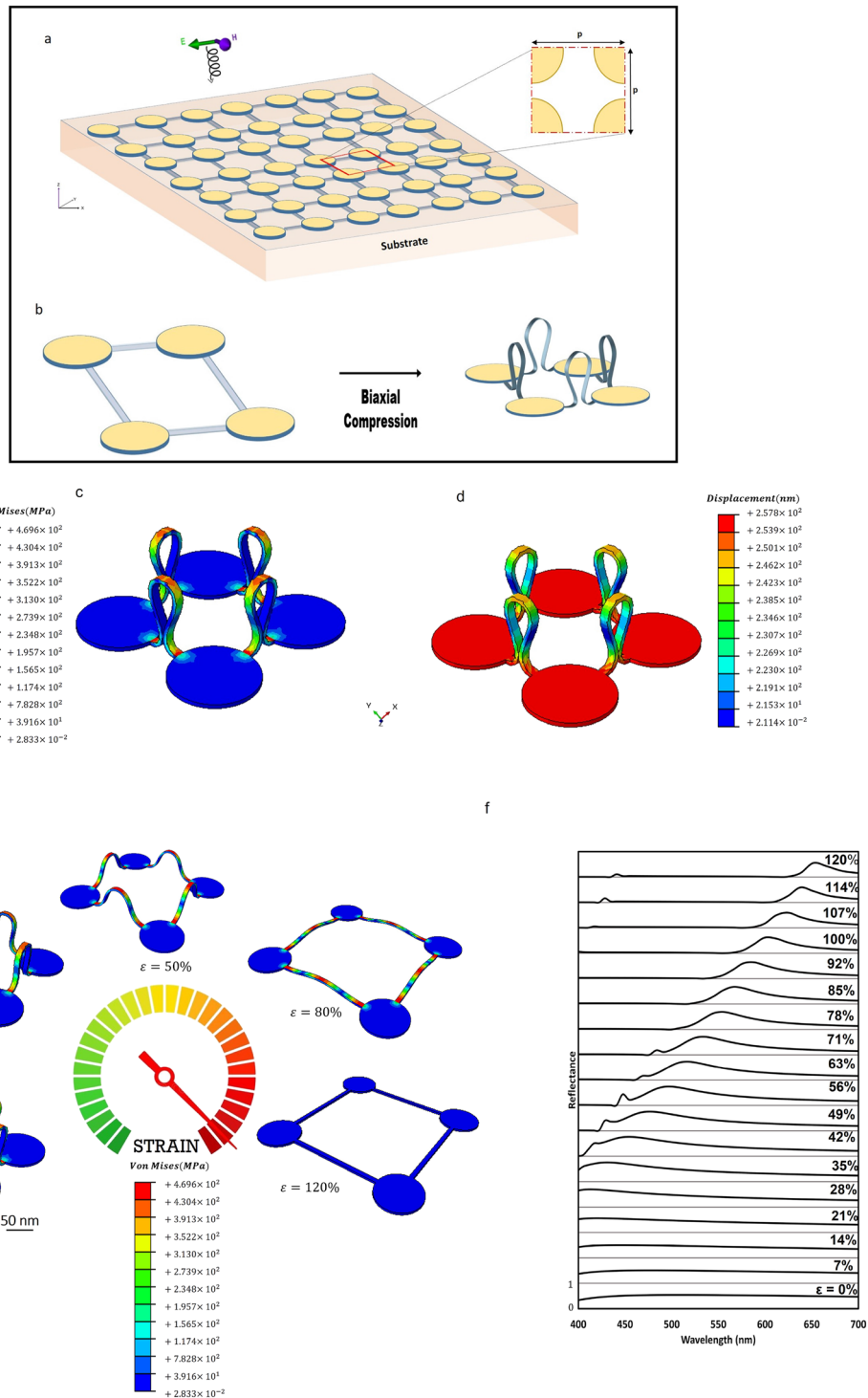


FIG. 2. (a) Schematic view of the geometry used in this study where a 2D array of Al nanodisks is located on a flexible site connected with thin bendable ribbons (PDMS). The yellow sites show the location of resonators fixed on the bottom substrate (moving in x and y directions). The whole structure is placed on a continuous substrate. The thickness of the disks is 100 nm. The period of the unit cell is $p = 280$ nm. The metasurface unit cell consists of four Al nanodisks each with a diameter $d = 200$ nm arranged in a square lattice. (b) The unit cell of the geometry in rest (left) and extreme (right) states. (c) von Mises stress and (d) strain distribution of the original pattern in the buckling process; (e) stress distribution and (f) the peak shift in the reflection curves as a function of wavelength in different levels of applied strain.

TABLE I. Comparison of various types of stretchable optical MMs.

Materials	Shape of resonator	Dimensions (nm)	Arrangement	Maximum strain (%)	Reference
Al/PDMS	Rectangular	$P^a 400-W^b 100-L^c 130-H^d 35$	Squared	32	11
Al/PDMS	Disk	$P320-D^e 200-H100$	Squared	31.6	17
Au/PDMS	Split ring	$L1 = L2 = 2.4 \mu\text{m}$...	5	30
TiO ₂ /PDMS	Squared	$P300-W230-H480$	Squared	30	12
Au/PDMS	Rectangular	$W100-L240-H70$	Triangular	30	31
Si/PDMS	Disk	$P490-D305-H480$	Squared	36	29
Au-PS/PDMS	Sphere	D1500	Hexagonal	20	32
Au/PDMS	Sphere	D11	Close-packed	20	33
Silver/PDMS	Grating	P665	...	23	34

^aPeriodicity.^bWidth.^cLength.^dThickness.^eDiameter of the resonator.

Here, we propose a universal design that allows rigid and soft materials to be paired without any limitations on stretchability and function. This design utilizes kirigami-inspired mechanical MMs and minimizes stress at the interface between the flexible substrate and resonators. As a result, reversible flexibility can be obtained over a wide range of strains, even above 120%. The details of the experiment procedure can be found in the supplementary material.

II. RESULTS

A. Mechanical simulation

Figures 2(a) and 2(b) show the kirigami architecture designed in this work. The geometry consists of a square lattice of Al nanodisks laying on a kirigami-based polymeric substrate. Each nanodisk is connected to the four neighboring nanodisks via a flexible ribbon made of polydimethylsiloxane (PDMS). The whole structure is placed on a pre-strained continuous supporting elastomeric substrate. The plasticity of the substrate, as a critical property for the shaping and forming of materials, depends on geometrical parameters such as the width ratio and thickness ratio.^{47,48} We tuned the width ratio, w/d (width of interconnections/diameter of disks), to control the local bending stiffness and designed an “infinitely deformable optomechanical MM.” Our calculation shows that a minimum width ratio ($w/d \geq 0.05$) is required to create an out-of-plane deformation of the interconnections; otherwise, the ribbons deform in the plane (2D) (Figs. A1 and A2, supplementary material). The width ratio was set at 0.1.

As the bi-axial pre-strain is released, stress is localized in the middle and both ends of the flexible ribbons where the bending stiffness is lower than that of the parts that host the resonators [cf. Fig. 2(c)]. This stress redistribution in the optimized geometry leads to a 2D-to-3D shape transformation, altering the interparticle distance in a controllable manner. It is worth mentioning that the bending-induced strain must remain below the maximum endurance limit for flexible connections.⁴⁶

The von Mises stress and strain distribution of the geometry under a biaxial strain of 120% is presented in Figs. 2(c) and 2(d).

In comparison to the previously studied geometries where rigid resonators were located on a continuous polymeric substrate, the stress concentration detaches from the interface to the ribbon-membrane connections [Fig. 2(c)]. This engineered strain localization is accompanied by huge out-of-plane deformation in the interconnections and a significant in-plane one in disks. Figure 2(e) shows the displacement of the resonators as the strain varies from 0% to 120%.

B. Optical simulation

The reflectance spectra of the geometry at various levels of strain are presented in Fig. 2(f). The applied biaxial strain along the planar direction of the substrate changes the period of the unit cell equally in both x and y directions, thus shifting the surface plasmon resonance. Interestingly, the stress distribution in various strain levels shows how the stress concentration is relocated from the interface to the flexible connections [cf. Fig. 2(e)]. The rest and extreme states correspond to the minimum gap = 80 nm ($\epsilon = 0\%$) and the maximum gap = 420 nm ($\epsilon = 120\%$), respectively. Since this geometry preserves symmetry, by stretching the structure, the original single resonance mode moves to a higher wavelength [cf. Fig. 2(f)].

The reflectance spectra of resonators are very sensitive to the gap size (Fig. A3) so much that when the gap size is smaller than 192 nm ($\epsilon < 40\%$), the two separated reflectance peaks combine together and form a single wide peak. As a matter of fact, by minimizing the gap, the TM polarized incidence excites electric dipoles (EDs) along the disk dimer axis, inducing the bonding electric–electric dipole interaction, similar to the plasmonic dimer case.⁴⁹ This interaction can lower the energy of the exciting electric dipoles, resulting in a redshift of the resonant wavelength of the electric mode (left peak), as shown in Fig. 2(f). At the same time, the magnetic dipoles (MDs) are excited in each particle but perpendicular to the dimer axis. The repulsive force between the poles in the particles increases the energy level of the magnetic mode, leading to a blue shift of the resonant wavelength (right peak). Such opposite peak shifts cause a single wide resonance, which is centered at $\lambda = 508$ nm due to two plasmonic hybridized modes with different local fields in the z -direction⁵⁰ [cf. Figs. A4(b)–A4(d)]. The single

resonance is close to the localized surface plasmon (LSP) resonance of a single disk, as observed elsewhere.⁵¹

A contour map of the reflectance is presented in Fig. 3(a) to summarize the relative contributions made by different phenomena [i.e., surface plasmon resonance (PSPR) and LSP resonance] pertaining to different metal–substrate interfaces. For the case of minimum gap (strain), the PSPR dominates the mechanism, leading to a broad bandwidth spectrum.¹¹ The full width at half maximum (FWHM) at different strain levels is shown in Fig. 3(b). The results show that the proposed geometry can provide sharp peaks at a higher strain level. For instance, for $\epsilon = 120\%$, the FWHM decreases to 33.1 nm, which is 5.1 times smaller than its conventional counterparts ($\epsilon = 36\%$). Here, the reflectance of the Al nanodisks is affected by both the magnetic dipole (MD) resonance and the electric dipole (ED) resonance. The intensity of the electric field around the Al nanodisk as a function of strain level under longitudinal polarization for the two observed reflectance peaks at 440 and 651 nm is presented in Fig. 3(c). For the ED resonance, for strains below 40%, the electrical field distributed outside the nanodisks fairly increases by increasing the gap. However, when the strain level exceeds 40% (gap = 192 nm), the single hybridized peak splits into two narrow ones, reducing the ED-induced electric field. In contrast, the MD

resonance is observed to red-shift significantly from 440 nm at a 192 nm gap to 651 nm at a 420 nm gap, which forms a field enhancement in the disk's edges (The magnetic field distribution is provided in Fig. A4, supplementary material).

III. DESIGN AND PROPERTY OPTIMIZATION

The design of a “single geometry” with a dynamic and broad-range modulation of absorption, reflection, and transmission of an electromagnetic wave is still highly demanded. Plasmonics supplies stronger field enhancements, making them special for designing high-resolution colorimetric sensing applications.^{52–54} Structural coloration has progressed significantly, but the absence of a wide real-time tunability and reversible coloration schemes has slowed down the progression in some relevant areas.⁵⁵ Conventional design optimization techniques such as numerical simulations usually require time-consuming data acquisition or complicated reconstruction algorithms for data post-processing, making them largely ineffective for complex calculations.⁵⁶ Recently, the emergence of the deep learning (DL) technique has revolutionized the prediction of complex systems' performance. DL is a sub-category

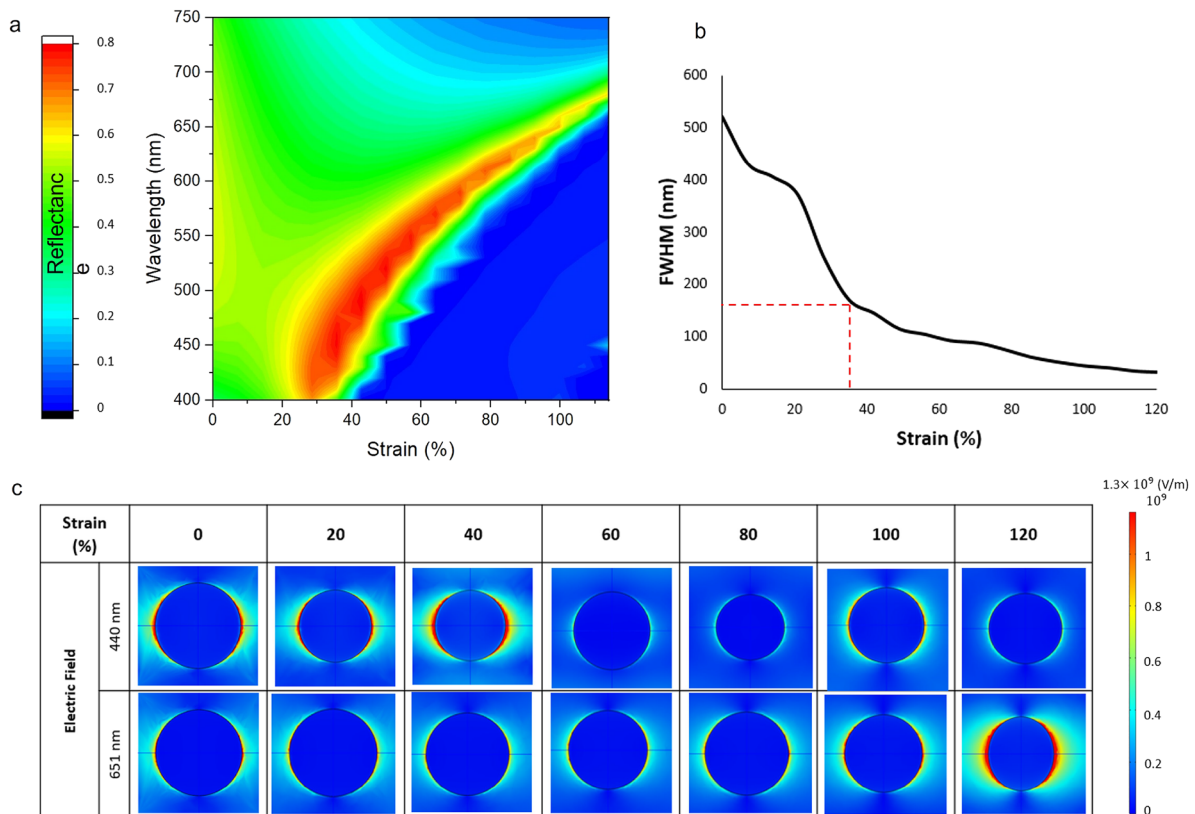


FIG. 3. (a) Contour map of the calculated reflective spectra; (b) FWHM values as a function of applied strain. The red dashed line presents the calculated FWHM (171 nm) at the maximum strain (36%) level in conventional geometry. (c) Electric field distribution in the x, y plane for nanodisks at incident wavelengths of 440 and 651 nm, corresponding to peaks revealed in simulation results.

of machine learning (ML), which automatically infers a basic relationship between different variables to extract the key features based solely upon observed data. Here, an optimized fully connected deep neural network (DNN) is developed to predict the structural color parameters,⁵⁶ where the mechanically induced deformation, ϵ , and

geometrical parameters including the thickness of the resonator (Al), H, and the diameter of the disk, D, are tuned [cf. Fig. 4(a)]. DNNs are normally used for regression-type problems to take continuous values.⁵⁷ Table II presents the range of variables for both training and optimization in this work. A total of 2100 data were

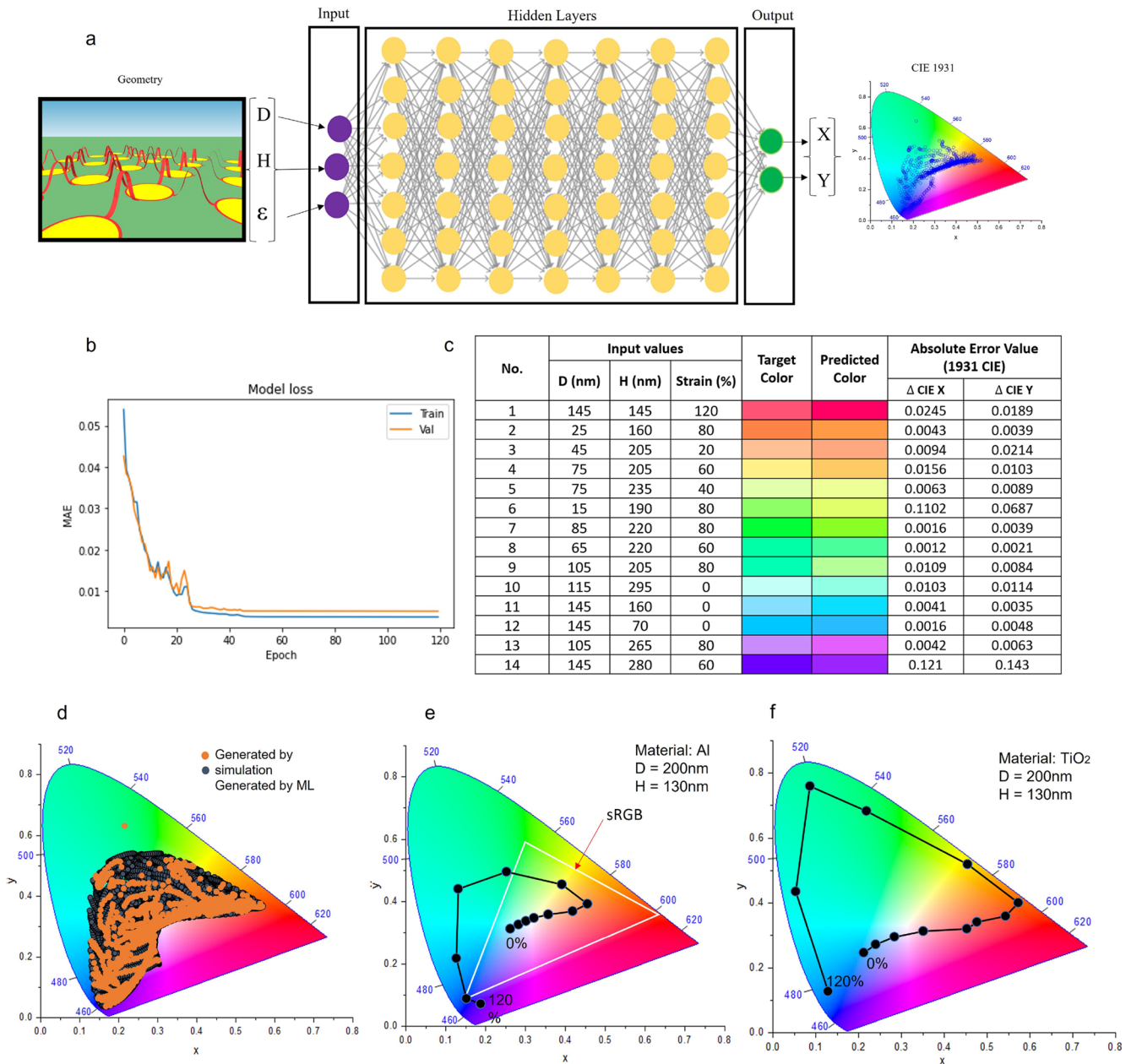


FIG. 4. (a) Schematic of a fully connected DNN that extracts the complex relationship between mechanical and geometrical parameters and structural color parameters plotted on the CIE 1931 gamut. (b) The learning curve of the DNN. (c) Comparison of the prediction accuracy of 14 random target structural colors. (d) CIE chromaticity diagrams of the samples derived from FEM (orange) and ML (black). (e) The optimized geometry comprising an Al nanodisk (H = 130 nm and D = 200 nm) exhibits 27.65% coverage of the sRGB color space. The white triangle depicts the standard RGB (sRGB) color triangle. (f) CIE 1931 chromaticity diagrams overlaid with points corresponding to the reflectance spectra colors of the optimized geometry consisting of a TiO₂ nanodisk (H = 130 nm and D = 200 nm) subjected to various strain levels.

18 August 2023 10:01:15

TABLE II. Range of variables for training the DNN and optimization.

Variables	Training			Optimization		
	Range	Step	No. of samples	Range	Step	No. of samples
Strain (ϵ) (%)	0–120	20	7	0–120	10	13
Height of Al (H) (nm)	5–145	10	15	5–145	5	29
Diameter of the disk (D) (nm)	10–295	20	20	10–295	5	58
Total			2100			21 866

extracted using a combination of optical and mechanical simulations, generating a wide range of colors to train the network. Such small-scale data were generated carefully to not only ensure enough diversity to train the network but also encapsulate enough similar data that provide full mapping of input and output.

Figure 4(b) shows that training curves converge with a 10^5 order of magnitude decrease in computational time in comparison to FEM simulations. Figure 4(c) presents the high accuracy of the DNN model in predicting 14 random modes, providing a wide range of colors. These results show that the presented DL method is able to accurately interpolate the complex relationship between the geometrical parameters of the optomechanical metamaterials and color in various levels of strain. The trained model was then used to predict the structural color parameters (X, Y) for 21 866 samples based on Table II. Figure 4(d) compares the scattering pattern of the samples derived from FEM and ML. As was shown, the sweeping of the key parameters with smaller steps allows finding more geometries, which offer a wider color gamut, especially in the green and blue areas. Finally, we found the optimized single geometry consisting of Al nanodisks with a height of 130 nm and a diameter of 200 nm that provides the widest areal color space coverage, taking up 27.65% of standard red-green-blue (sRGB) space [cf. Fig. 4(e)].

The proposed universal geometry has a high potential to enlarge the color coverage in dielectric-based structural color systems so that replacing the plasmonic component with a high dielectric material, such as TiO_2 , provides a wide range of colors in the CIE 1931 chromaticity diagram. As shown in Fig. 4(f), the single proposed design generates a full-color palette ranging from white to red, green, and blue.

IV. CONCLUSIONS

This study proposes highly stretchable optomechanical MMs using a universal kirigami-induced geometry with 120% stretchability, which provides reversible resonance peak shifts and relocates stress concentration from the interface to the flexible sections. A deep neural network was also trained using a small dataset taken from optical and mechanical simulations to extract the geometrical features of the optimized design, providing the widest color gamut with a 10^5 order of magnitude decrease in computational time. This method can be used to make active metamaterials suitable for wearable sensors and optoelectronic devices.

SUPPLEMENTARY MATERIAL

See the supplementary material for details of various geometries, experimental procedures, and optical performance of the proposed design.

ACKNOWLEDGMENTS

This study was funded by the DDS and the Department of Engineering at Durham University.

AUTHOR DECLARATIONS

Conflict of Interest

The authors have no conflicts to disclose.

Author Contributions

Amir Ghasemi: Data curation (lead); Formal analysis (lead); Investigation (lead); Methodology (equal); Writing – original draft (lead); Writing – review & editing (equal). **Rui Fang:** Investigation (supporting); Writing – review & editing (supporting). **Dagou A. Zeze:** Funding acquisition (supporting); Investigation (supporting); Supervision (supporting); Writing – review & editing (supporting). **Mehdi Keshavarz Hedayati:** Conceptualization (lead); Funding acquisition (lead); Investigation (lead); Methodology (lead); Project administration (lead); Resources (lead); Supervision (lead); Writing – original draft (supporting); Writing – review & editing (lead).

DATA AVAILABILITY

The data that support the findings of this study are available from the corresponding author upon reasonable request.

REFERENCES

- ¹N. Yu and F. Capasso, *Nat. Mater.* **13**, 139 (2014).
- ²F. Liu, A. Ptilakis, M. S. Mirmoosa, O. Tsilipakos, X. Wang, A. C. Tasolamprou, S. Abadal, A. Cabellos-Aparicio, E. Alarcón, C. Liaskos *et al.*, in *2018 IEEE International Symposium on Circuits and Systems (ISCAS)* (IEEE, 2018), pp. 1–5.
- ³B. O. Asamoah, “Light and matter interactions on plasmonic platforms,” Ph.D. thesis, Itä-Suomen yliopisto, 2021.

- ⁴M.-X. Ren, W. Wu, W. Cai, B. Pi, X.-Z. Zhang, and J.-J. Xu, *Light: Sci. Appl.* **6**, e16254 (2017).
- ⁵W. Xu, T. J. Lu, and F. Wang, *Int. J. Solids Struct.* **47**, 1830 (2010).
- ⁶S. Wu, Q. Ze, R. Zhang, N. Hu, Y. Cheng, F. Yang, and R. Zhao, *ACS Appl. Mater. Interfaces* **11**, 41649 (2019).
- ⁷Y. Ke, I. Balin, N. Wang, Q. Lu, A. I. Y. Tok, T. J. White, S. Magdassi, I. Abdulhalim, and Y. Long, *ACS Appl. Mater. Interfaces* **8**, 33112 (2016).
- ⁸M. K. Hedayati, M. Javaheri, A. U. Zillohu, H. J. El-Khozondar, M. S. Bawa'aneh, A. Lavrinenko, F. Faupel, and M. Elbahri, *Adv. Opt. Mater.* **2**, 705 (2014).
- ⁹J. Eaves-Rathert, E. Kovalik, C. F. Ugwu, B. R. Rogers, C. L. Pint, and J. G. Valentine, *Nano Lett.* **22**, 1626 (2022).
- ¹⁰S. Chen, J. Chen, X. Zhang, Z.-Y. Li, and J. Li, *Light: Sci. Appl.* **9**, 75 (2020).
- ¹¹M. L. Tseng, J. Yang, M. Semmlinger, C. Zhang, P. Nordlander, and N. J. Halas, *Nano Lett.* **17**, 6034 (2017).
- ¹²C. Zhang, J. Jing, Y. Wu, Y. Fan, W. Yang, S. Wang, Q. Song, and S. Xiao, *ACS Nano* **14**, 1418 (2019).
- ¹³N. Jeon, J. Noh, C. Jung, and J. Rho, *New J. Phys.* **24**, 075001 (2022).
- ¹⁴C.-W. Lee, H. J. Choi, and H. Jeong, *Nano Convergence* **7**, 3 (2020).
- ¹⁵S. Chen, E. S. Kang, M. Shiran Chaharsoughi, V. Stanishev, P. Kühne, H. Sun, C. Wang, M. Fahlman, S. Fabiano, V. Darakchieva, and M. P. Jonsson, *Nat. Nanotechnol.* **15**, 35 (2020).
- ¹⁶X. Fan, Y. Li, S. Chen, Y. Xing, and T. Pan, *Small* **16**, 2002484 (2020).
- ¹⁷S. Song, X. Ma, M. Pu, X. Li, K. Liu, P. Gao, Z. Zhao, Y. Wang, C. Wang, and X. Luo, *Adv. Opt. Mater.* **5**, 1600829 (2017).
- ¹⁸Z. Xu and Y. S. Lin, *Adv. Opt. Mater.* **7**, 1900379 (2019).
- ¹⁹J. Morris Jr., C. Krenn, D. Roundy, and M. L. Cohen, *Mater. Sci. Forum.* **426**, 4429 (2002).
- ²⁰S. Xu, T. Odaira, S. Sato, X. Xu, T. Omori, S. Harjo, T. Kawasaki, H. Seiner, K. Zoubková, Y. Murakami, and R. Kainuma, *Nat. Commun.* **13**, 5307 (2022).
- ²¹W. H. Robinson and S. D. Truman, *J. Mater. Sci.* **12**, 1961 (1977).
- ²²S. S. Brenner, *J. Appl. Phys.* **27**, 1484 (1956).
- ²³G. L. Pearson, W. T. Read, Jr., and W. L. Feldmann, *Acta Metall.* **5**, 181 (1957).
- ²⁴N. Tada, Y. Hu, T. Uemori, and T. Nakata, in *MATEC Web of Conferences* (EDP Sciences, 2017), Vol. 108, p. 01004.
- ²⁵T. Li, Z. Y. Huang, Z. C. Xi, S. P. Lacour, S. Wagner, and Z. Suo, *Mech. Mater.* **37**, 261 (2005).
- ²⁶T. Badloe, J. Lee, J. Seong, and J. Rho, *Adv. Photonics Res.* **2**, 2000205 (2021).
- ²⁷T. Baëtens, E. Pallicchi, V. Thomy, and S. Arscott, *Sci. Rep.* **8**, 9492 (2018).
- ²⁸N. Bowden, S. Brittain, A. G. Evans, J. W. Hutchinson, and G. M. Whitesides, *Nature* **393**, 146 (1998).
- ²⁹X. Zhang, Y. Zhou, H. Zheng, A. E. Linares, F. C. Ugwu, D. Li, H.-B. Sun, B. Bai, and J. G. Valentine, *Nano Lett.* **21**, 8715 (2021).
- ³⁰J. B. Reeves, R. K. Jayne, T. J. Stark, L. K. Barrett, A. E. White, and D. J. Bishop, *Nano Lett.* **18**, 2802 (2018).
- ³¹H.-S. Ee and R. Agarwal, *Nano Lett.* **16**, 2818 (2016).
- ³²X. Zhu, S. Xiao, L. Shi, X. Liu, J. Zi, O. Hansen, and N. A. Mortensen, *Opt. Express* **20**, 5237 (2012).
- ³³Y.-L. Chiang, C.-W. Chen, C.-H. Wang, C.-Y. Hsieh, Y.-T. Chen, H.-Y. Shih, and Y.-F. Chen, *Appl. Phys. Lett.* **96**, 041904 (2010).
- ³⁴S. Olcum, A. Kocabas, G. Ertas, A. Atalar, and A. Aydinli, *Opt. Express* **17**, 8542 (2009).
- ³⁵J. A. Fan, W.-H. Yeo, Y. Su, Y. Hattori, W. Lee, S.-Y. Jung, Y. Zhang, Z. Liu, H. Cheng, L. Falgout *et al.*, *Nat. Commun.* **5**, 3266 (2014).
- ³⁶M. D. Ho, Y. Liu, D. Dong, Y. Zhao, and W. Cheng, *Nano Lett.* **18**, 3593 (2018).
- ³⁷T. Someya, Y. Kato, T. Sekitani, S. Iba, Y. Noguchi, Y. Murase, H. Kawaguchi, and T. Sakurai, *Proc. Natl. Acad. Sci. U. S. A.* **102**, 12321 (2005).
- ³⁸P. Won, J. J. Park, T. Lee, I. Ha, S. Han, M. Choi, J. Lee, S. Hong, K. J. Cho, and S. H. Ko, *Nano Lett.* **19**, 6087 (2019).
- ³⁹Y. Gao and L. Wang, *Compos. Struct.* **291**, 115586 (2022).
- ⁴⁰W. Wu, W. Hu, G. Qian, H. Liao, X. Xu, and F. Berto, *Mater. Des.* **180**, 107950 (2019).
- ⁴¹H. Yu, H. Wang, B. Liang, and X. Guo, *Extreme Mech. Lett.* **49**, 101436 (2021).
- ⁴²J. U. Surjadi, L. Gao, H. Du, X. Li, X. Xiong, N. X. Fang, and Y. Lu, *Adv. Eng. Mater.* **21**, 1800864 (2019).
- ⁴³T. Ranzani, S. Russo, N. W. Bartlett, M. Wehner, and R. J. Wood, *Adv. Mater.* **30**, 1802739 (2018).
- ⁴⁴C. Wang, D. Zhang, J. Li, and Z. You, *Int. J. Solids Struct.* **251**, 111752 (2022).
- ⁴⁵H. Zhang and J. Paik, *Adv. Funct. Mater.* **32**, 2107401 (2022).
- ⁴⁶Y. Zhang, Z. Yan, K. Nan, D. Xiao, Y. Liu, H. Luan, H. Fu, X. Wang, Q. Yang *et al.*, *Proc. Natl. Acad. Sci. U. S. A.* **112**, 11757 (2015).
- ⁴⁷Y. Shi, F. Zhang, K. Nan, X. Wang, J. Wang, Y. Zhang, Y. Zhang, H. Luan, K. C. Hwang, Y. Huang *et al.*, *Extreme Mech. Lett.* **11**, 105 (2017).
- ⁴⁸Z. Yan, F. Zhang, J. Wang, F. Liu, X. Guo, K. Nan, Q. Lin, M. Gao, D. Xiao, Y. Shi *et al.*, *Adv. Funct. Mater.* **26**, 2629 (2016).
- ⁴⁹E. Prodan, C. Radloff, N. J. Halas, and P. Nordlander, *Science* **302**, 419 (2003).
- ⁵⁰S. Chen, W. Wei, Z. Liu, X. Liu, S. Feng, H. Guo, and J. Li, *Photonics Res.* **8**, 1177 (2020).
- ⁵¹W. Li, K. Ren, and J. Zhou, *TrAC, Trends Anal. Chem.* **80**, 486 (2016).
- ⁵²R. Fang, A. Ghasemi, D. A. Zeze, and M. Keshavarz Hedayati, *J. Appl. Phys.* **132**, 133102 (2022).
- ⁵³X. Zhu, J. Engelberg, S. Remennik, B. Zhou, J. N. Pedersen, P. Uhd Jepsen, U. Levy, and A. Kristensen, *Nano Lett.* **22**, 2786 (2022).
- ⁵⁴J. S. Clausen, E. Højlund-Nielsen, A. B. Christiansen, S. Yazdi, M. Grajower, H. Taha, U. Levy, A. Kristensen, and N. A. Mortensen, *Nano Lett.* **14**, 4499 (2014).
- ⁵⁵Y. Lee, J. Kwon, J. Lim, W. Shin, S. Park, E. Hwang, J. Shin, H. Cho, J. Jung, H.-J. Kim *et al.*, *Adv. Funct. Mater.* **31**, 2006854 (2021).
- ⁵⁶N. B. Roberts and M. Keshavarz Hedayati, *Appl. Phys. Lett.* **119**, 061101 (2021).
- ⁵⁷S. Head and M. Keshavarz Hedayati, *Appl. Sci.* **12**, 4877 (2022).